Cluster Collapse in a Cylindrical Cell: Correlating Multibubble Sonoluminescence, Acoustic Pressure, and Erosion

Christopher J. B. Vian,[†] **Peter R. Birkin,**[†,*] **and Timothy G. Leighton**[‡]

School of Chemistry, and Institute of Sound and Vibration Research, University of Southampton, Hampshire SO17 1BJ, U.K.

Received: March 29, 2010; Revised Manuscript Received: July 16, 2010

A cylindrical ultrasonic reactor was driven at eight discrete frequencies in the range 20−150 kHz. Imaging of multibubble sonoluminescence (MBSL) within this cell showed discrete modes of activity throughout this frequency range. This modal activity was compared to the pressure distribution through the cell and also to the erosion/corrosion activity. The erosion/corrosion was detected using an electrochemical method employing a passivated aluminum electrode (250 μm diameter). Each erosion/corrosion event was counted over a fixed time period (specifically 30 s) and used to map this phenomenon throughout a region of the cell. A strong spatial correlation was shown between the MBSL imaging, the acoustic pressure, and the erosion mapping at relatively low ultrasonic frequencies (here <50 kHz). However, at higher frequencies, although MBSL activity and relatively high acoustic amplitudes were detected, the rate of the erosion/corrosion activity of the system decreased. High-speed imaging (>100000 fps) of a bubble cloud near the electrode surface showed a region of bubble activity, the dynamics of which were correlated to the erosion/corrosion transients produced. These observations contribute to the growing body of knowledge which will allow the development of ultrasonic cleaning systems optimized for particular scenarios.

Introduction

Cavitation is exploited in many laboratory and industrial situations. These range from the cleaning of instrumentation, processing of chemical species and materials (for example electrode surfaces) to the manufacture of mass-produced domestic products and foods.[1−3] In medicine, erosive cavitation is exploited in, for example, dentistry[4,5] and lithotripsy.[6] Clearly this phenomenon is of broad use in a number of different scenarios. However, the assessment of the effects of cavitation turns out to be an extremely difficult task to achieve in a definitive or absolute sense.[7] This is because cavitation produces a wide variety of different physical or chemical effects. In itself cavitation can also be subdivided into different categories. The simplest subdivision is the distinction between inertial (formerly referred to as ‘transient’ cavitation) and noninertial (formerly referred to as ‘stable’ cavitation) collapse of bubbles within a suitable pressure environment.[8] The assignment of a cavitation event is governed by the initial size of the bubble, the solution characteristics, and the temporal nature and amplitude of the pressure field employed. In an effort to decide on the type of cavitation likely to be produced by a particular experimental arrangement, Apfel and Holland produced a relatively simple model based on the response of a single bubble in relation to a sinusoidal pressure wave.[9−13] This study also linked experimental data to infer temperatures[14−19] within the core of the collapsing bubble (~5000 K) obtained through a variety of chemical and physical measurements (other temperature criteria, e.g. the 1550 K of Šponer,[20−22] give similar results to the 5000 K criterion[8,23]). Apfel and Holland also used other assessments linked to expansion (the ratio of the maximum expansion radius to the initial radius of a given bubble), such that, for example, a value in the range 2−2.3 appears to predict the inertial/noninertial border.[8] Using this criterion, bubbles with greater expansion ratios than the set value are assumed to undergo inertial cavitation, and those with smaller expansion ratios are assumed to undergo noninertial cavitation. The somewhat flexible terms in which the criteria (for temperature or expansion ratio) are couched should not be overly concerning, as the dramatic change in both as bubbles cross from noninertial to inertial character allows a broader tolerance in such criteria than if temperatures and expansion ratios were to scale linearly with, say, driving pressure. Because of this, the model of Apfel and Holland provides an extremely useful guide, so long as users recognize that it refers to the behavior of a single bubble in response to the pressure field at its location, and only the first few cycles of the bubble dynamics are captured. During a typical sonochemical tone-burst, some key events dominate at the onset of the pulse,[24,25] while others (such as rectified diffusion or motion induced by radiation forces) occur over time scales outside of the consideration of the Apfel/Holland model. Therefore, the inertial/noninertial model produced by Apfel and Holland for bubble responses to diagnostic ultrasound needs to be interpreted carefully for application to sonochemistry. Such application must be tempered by the acknowledgment that a sonochemical reactor contains many interacting bubbles with a wide range of sizes (which can change through dissolution, exsolution, fragmentation, and coalescence) and locations (which can change through bubble migration through turbulence, radiations forces, circulation, and buoyancy).[23] Although bubble simulations have suggested that bubble interactions may produce changes over the sub 10 μs scale,[26] longer times are required to encompass how clouds of bubbles evolved under the influences of degassing, buoyancy, radiation forces, bubble coalescence and fragmentation, turbulence and circulation, shielding of the ultrasound, etc.[3,27−29] These changes can occur outside of the

---

[*] Author for correspondence. E-mail: prb2@soton.ac.uk. Telephone: 00 44 2380 594172. Fax: 00 44 2380 593781.

[†] School of Chemistry.

[‡] Institute of Sound and Vibration Research.

10.1021/jp1027977

short time window of the Apfel/Holland model (during which, for example, rectified diffusion is usually negligible). Changes in size might take a bubble into or out of the size window where inertial cavitation can occur, if the *local* acoustic field is sufficiently strong, and changes in location can affect that local field. This is because, when tone-burst fields are set up within sonochemical reactors, the field will not be uniform (simple linear theory shows how the temporal zero-to-peak pressure change at a rigid vessel wall will be up to double the zero-to-peak acoustical pressure amplitude of the wave that was traveling toward that wall).[1] Hence, mapping of the pressure field is recommended, but this, too, may be misleading.[1] This is because the onset and degree of cavitation in a vessel depend on the spatial peak value of the time-varying sound fields, and if the hydrophone used to map the sound field has a sensitive area greater than this, that spatial peak will be underestimated. Even assuming that the acoustic field has been measured without such peak underestimations (through spatial averaging or neglect of harmonic energy as a result of limited receiver bandwidth), and even though the acoustic field is a prime driver in the response to a bubble of given size in a known gas/liquid system, it is usually an "effect of cavitation" which is measured as a quantification tool.[7] This is because, even were the true driving pressure field *in the absence of cavitation* to be known, the field impinging on another bubble is not this but rather the dynamically changing field produced when neighboring bubbles scatter, shield, refract, and re-emit pressure waves.[23,30] Furthermore, in a multibubble sonochemical reactor the initial bubble size is not known, and the "effect of cavitation" depends on other ephemera (such as chemical and solid contaminants in the nominal gas/liquid stated for the system). The walls of the vessel itself and the immersed parts of the transducer are in many ways solid contaminants, scattering the sound field and providing interfaces to support cavitation nucleation.

Consequently, most investigations would favor direct measurement of the "effect of cavitation" which is important to the end user (erosion, sonochemical yield, etc.), which we will term the 'end user effect'. If the latter is too inconvenient or difficult to measure, some proxy "effect of cavitation" (audio acoustic emissions, luminescence, sonochemical yield, etc.) could be used, provided that the quantification of this effect scales in a known way with the quantification of the 'end user effect'.[7] Several cavitational effects have individually been reported as useful in determining 'cavitation activity', including acoustic emission from the cavitation events, chemical yield from the system, erosion of solid materials and light emission (in both spatial and global senses).[7,31−34] However, each of these measurement criteria relies on different mechanisms and, as such, is unlikely to be absolute for all applications of cavitation in physical and chemical systems. Hence, in order to assess cavitation one should not solely rely on a single quantification technique; rather, one should exploit a number of different assessments to draw 'global' conclusions related to a specific application and ideally cross-calibrate sensors for cavitation[7] or calibrate cavitation effects against more standardized ones (e.g., dosimetry[35−37]). This is the subject of this manuscript where a set of observational measurements (specifically acoustic pressure, multibubble sonoluminescence, and erosion of electrode surfaces) are used and compared in a small (1 dm^3) multibubble cylindrical sonochemical reactor.

Cylindrical reactors have been used to study sonochemical processes.[38] The symmetrical shape of such reactors will tend to produce strong modes, such that the acoustic efficiency of the system no longer is dominated only by the free field resonance of the transducer (at which the strongest acoustic pressure amplitudes would be generated in the free field) but rather shaped by the frequency response of the system as a whole, including the loaded transducer, the vessel shape, its contents, and boundary conditions.[34,39] The contents and boundary conditions are the most difficult to establish. The common use of the rigid boundary condition for aqueous solutions in, say, PMMA containers is confounded by the fact that measurements and theory show that bubble-free water in PMMA pipes can have significantly different propagation speeds than the nominal 1500 m s^{-1} assumed for infinite volumes of bubble-free water.[40] When bubbles are added, they can either increase or decrease the sound speed[41] by varying amounts, depending on the exact details of the bubble size distribution present. Given that the bubble population in a sonochemical reactor is extremely dynamic and changeable, the observation of modes (as highlighted by cavitation luminescence) that are stable over many seconds is surprising proof that the inhomogeneous and rapidly changing bubble population nevertheless can impart to the reactor a single effective sound speed in order to define that mode. To account for this a 'population feedback' mechanism enabling a particular mode to be excited was proposed.[39] In this paper we employ a simple cylindrical cell and compare luminescent imaging (using image intensified cameras) in combination with acoustic measurements and surface erosion sensing in an effort to assess the performance of this cell over a series of different frequencies. We now present the results of this study.

Experimental Section

The cylindrical reactor consisted of a single-walled cylinder (3 mm wall thickness) polymethylmethacrylate (PMMA) 220 mm high and 100 mm in diameter (94 mm inner diameter) with a machined metal base sealed in the cylinder with a rubber O-ring and Teflon tape. The driving transducer (Morgan Matroc Ltd., 33 kHz resonance frequency) was bonded to the metal base using Epofix epoxy resin (Streurs). The electrical signal required to drive the reactor was generated using a Thurlby Thandar TG1010 function generator and amplified by a Brüel & Kjear 2713 Power amplifier. This setup had maximum zero-to-peak voltage amplitude of 150 V. The drive signal was monitored using an oscilloscope.

The low intensity of light generated by multibubble sonoluminescence (MBSL) makes the use of standard photographic equipment impractical. Consequently, a low-light camera system constructed in-house and using a separate image intensifier and video camera was used as recorder. The unit consisted of a c-mount lens (25 mm Schneider f-stop 0.95) focusing the image onto the three-stage phosphor intensifier (Photek MCP325 intensifier controlled by a Photek MCPU-2.3 control unit) the image which was recorded using a JAI CV-A50 CCD camera connected to a Cyberoptics Imagenation PXC200A capture card in a PC. The images were recorded using in-house software based on the manufacturer-supplied software and adapted in Visual Basic 6. The Photek intensifier setup was capable of producing a luminous gain of the order of 2×10^7 compared to a normal CCD camera. To reduce the effects of random noise in the images, multiple images were stacked and/or averaged using Tambaware Software Image Stacker, V 1.03. Errors in position of bands of luminescence and timing of erosion events are included in the text. These are estimated by considering the accuracy of the images obtained and the shape of the current time transients respectively.

The pressure measurements were carried out using a Gras Type 10 CT hydrophone connected to a Brüel & Kjaer 2635

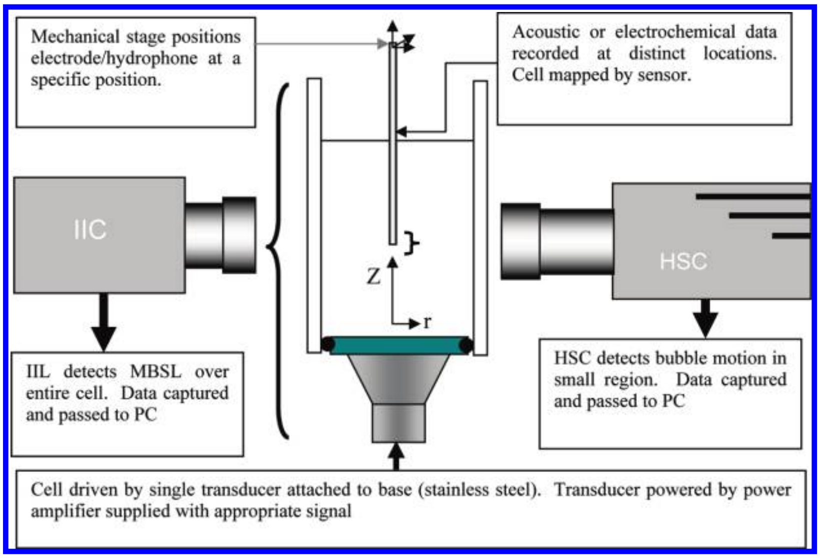

Figure 1. Schematic of the experimental setup employed in this work. This was used for erosion/corrosion, acoustic, imaging (both high-speed camera (HSC) and image-intensified camera (IIC)) of the cylindrical reactor. Note the HSC and the IIC are used under different lighting conditions. In addition the area imaged by each technique is different (see later data). The coordinate system (rZ) is added for clarity. The open bracket shows the region addressed by the high-speed camera.

charge amplifier. The hydrophone was taped to an 8 mm glass rod which was then mounted on a single-axis positioner (Parker L25i positioner) and the pressure scanned vertically through the cell. The hydrophone was scanned 100 mm in 2 mm increments; starting with the tip of the hydrophone 10 mm from the base of the reactor, placing the center of the hydrophone 20 mm from the base. The pressure at each point was recorded using a Measurement Computing PCI-DAS 4020/12 ADC card in a computer with the pressure amplitude extracted using a Visual basic program. The reactor was scanned in four locations: the central axis and at 10, 20, and 25 mm from the central axis. All four measurements were carried out in the same plane within the reactor, as the reactor was considered to have rotational symmetry around the central axis.

Figure 1 shows the general configuration of the cell and associated measurements. Note these experiments are not all performed simultaneously, owing to the constraints (e.g., lighting level) required for some techniques.

Electrochemical surface erosion/corrosion measurements were made on a 250 μm diameter Al electrode sealed in epoxy resin (Streurs Epofix) held at 0 V with respect to a stainless steel counter/reference electrode. This enabled the aluminum electrode to be held in the passive state ready to detect erosion of the surface as a corresponding corrosion transient (see refs 31−33, 42, and 43 for more details). The signal from the electrode was processed using an in-house current follower and recorded using an oscilloscope (LeCroy 9310AM). Counting measurements were made using a multichannel analyzer (Pocket MCA 8000A Multi Channel Analyzer (MCA)). The MCA recorded over a period of 30 s (4096 levels over 5 V). The threshold for peak detection was set at channel 200 corresponding to a trigger voltage of 244 mV or peak height of 2.44 μA. The position of the electrode within the reactor was controlled using the same apparatus as for the pressure measurements. To control the scanning process, a Visual Basic 6 program was written that controlled the MCA and automated positioner and provided a gating pulse to operate the drive signal for the reactor. The gating pulse for the drive signal was required, owing to the prolonged period of time required for the MCA to transfer data to the PC (>30 s, longer than the acquire time). During this data transfer period, the drive signal was terminated to the reactor, hence avoiding the likelihood that there would be significant changes in the temperature and other conditions within the reactor as a result of continuous insonification.

High-speed imaging was used to understand further the processes involved in the removal and then reformation of passivated oxide layers on electrodes. Imaging was conducted using a Photron APX-RS camera and a Navitar 12X Zoom c-mount lens connected to a PC by means of a firewire (IEEE 1394) cable. The camera was mounted on an XY stage, enabling the easy positioning of the camera and ensuring an accurate focus could be attained. The images were analyzed using Photron Fastcam Viewer software, version 2.4.3.8. Illumination was provided by a Fostec DCR 150W light source positioned such that the image reaching the camera was a silhouette. Electrochemical information was recorded on a Le Croy 9310 digital oscilloscope connected to a PC using a GPIB port. To ensure simultaneous recording of the high-speed imagery and the electrochemistry the signal from the electrochemistry was monitored by a PC-based ADC card (National Instruments PCI-6025E), and when the magnitude of the current from the electrochemistry exceeded a trigger value (signifying the presence of an event), a TTL pulse was sent to the camera and oscilloscope to trigger them.

For all experiments 1 dm^3 of aerobic 0.1 mol dm^{-3} Na_2SO_4 solution was used. This enabled the surface of the aluminum electrode to be passive under the conditions employed and provided ionic conductivity for the electrochemical signals detected. This was made up using water from a USF Elga Purelab Option E10 water purification system. Water purified in this manner had a resistivity above 15 MΩ cm and a low organic content (manufacture quoted TOC < 30 ppb). Na_2SO_4 (Fisher, LRG) was used without further purification. The height of solution within the cell was 14.4 cm.

Results and Discussion

The cylindrical cell can be imaged under low-light conditions in order to ascertain frequencies where high cavitation activity (here denoted as regions of high MBSL output) is observed (similar MBSL bands in a MHz field of a physiotherapy device were shown to occur at acoustic pressure antinodes[29] and

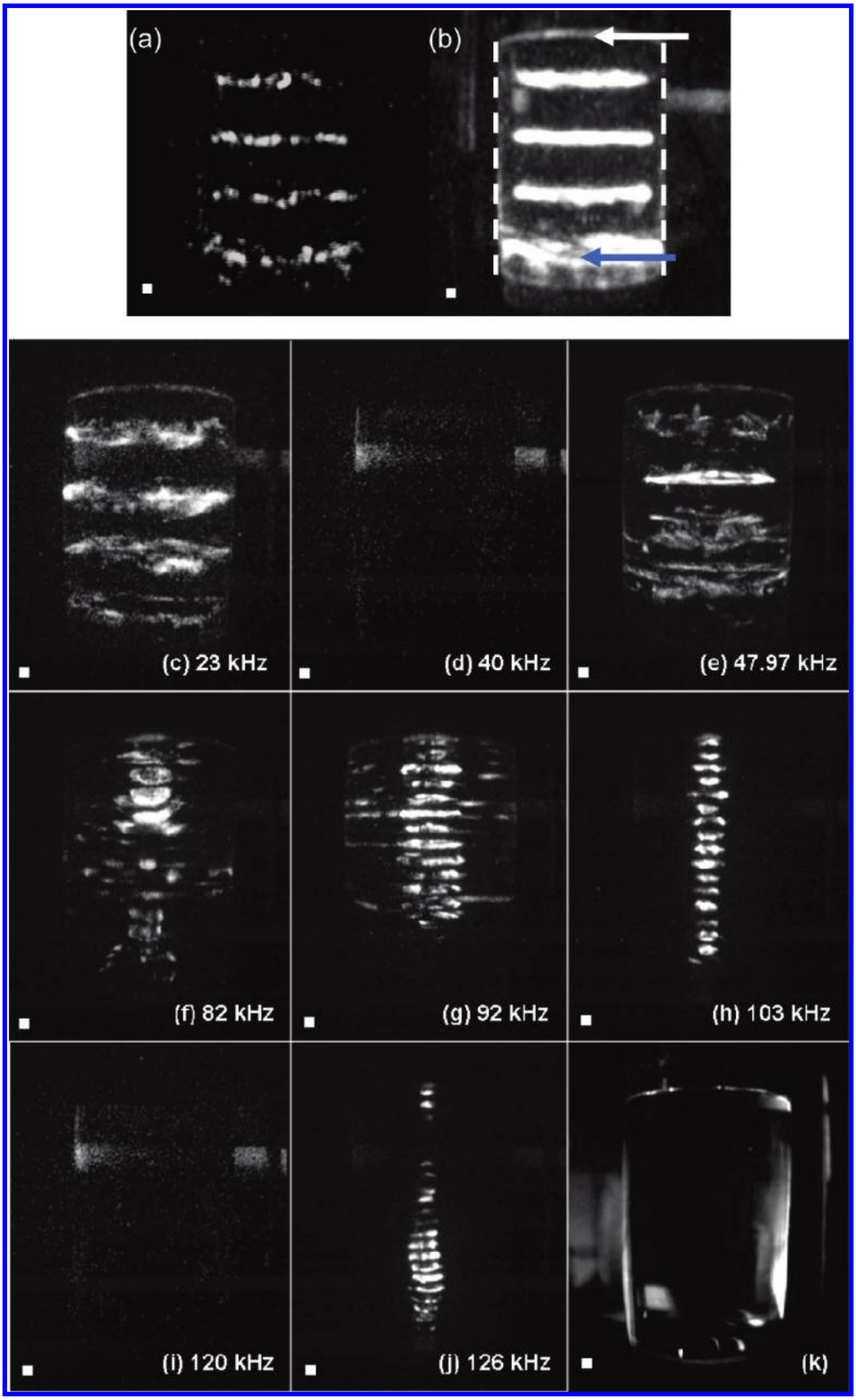

Figure 2. Images of the cylindrical reactor containing 1 dm^3 of water driven at 23 kHz and at 150 V_{AC} (~250 kPa zero-to-peak amplitude). (a) Single image recorded using the Photek intensifier system. (b) Amalgamation of 94 consecutive images recorded under the same conditions. The amalgamation was achieved using image stacking software (see Experimental Section). The white arrow indicates the air/water boundary, the blue arrow, the base of the cell, and the dotted vertical lines, the walls of the cell. MBSL images of the reactor at different drive frequencies. Images correspond to (c) 23 kHz, (d) 40 kHz, (e) 47.97 kHz, (f) 82 kHz, (g) 92 kHz, (h) 103 kHz, (i) 120 kHz, (j) 126 kHz, and (k) reactor with light up. Reactor contained 1 dm^3 of 0.1 mol dm^{-3} Na_2SO_4 solution and was driven at 150 V (zero-to-peak). Images are a stacked composite of over 100 images. The size of the active element of the hydrophone used in this study is included in each image as a white square in the bottom left of each frame.

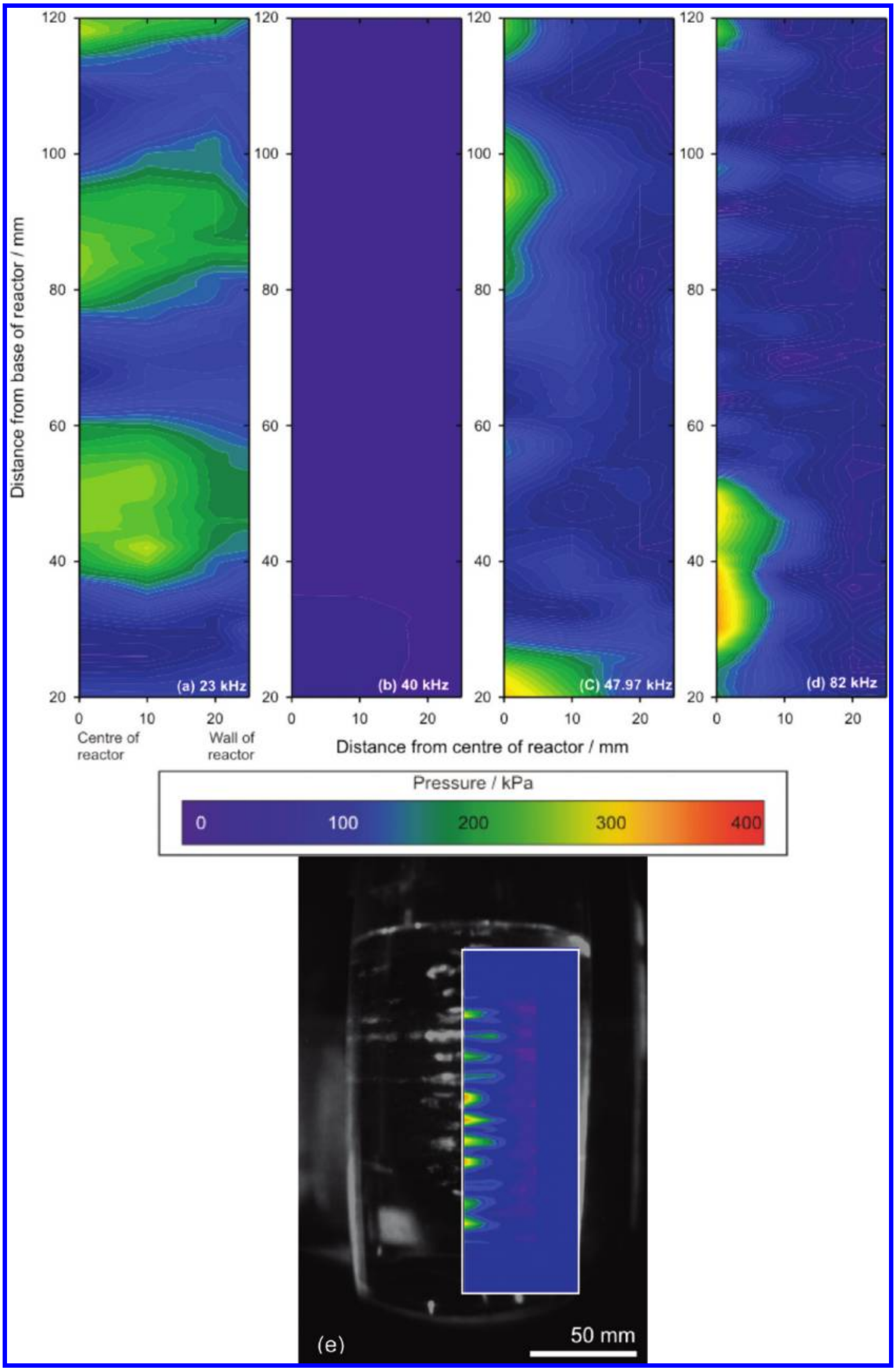

Figure 3. Zero-to-peak pressure contour maps of the cylindrical reactor driven at 23, 40, 47.97, and 82 kHz corresponding to maps (a), (b), (c), and (d), respectively. Each map is derived from four vertical scans with a resolution of 2 mm at 0, 10, 20, and 25 mm from the central axis of the reactor. The reactor contained 1dm^3 of 0.1 mol dm^{-3} Na$_2$SO$_4$ and was driven at 150 V zero-to-peak amplitude in each case. (e) Composite image of the cylindrical reactor showing the low-light emission image when driven at 92 kHz (black and white) with the corresponding zero-to-peak acoustic pressure contour map (color) to show the correlation between the two measurements.

correlated with the locations of maximum cell death). Figure 2 shows an example of the data that can be gathered from this procedure. Note that at the low-frequency region investigated ($\sim$20−50 kHz), the luminescent activity of this cylindrical cell

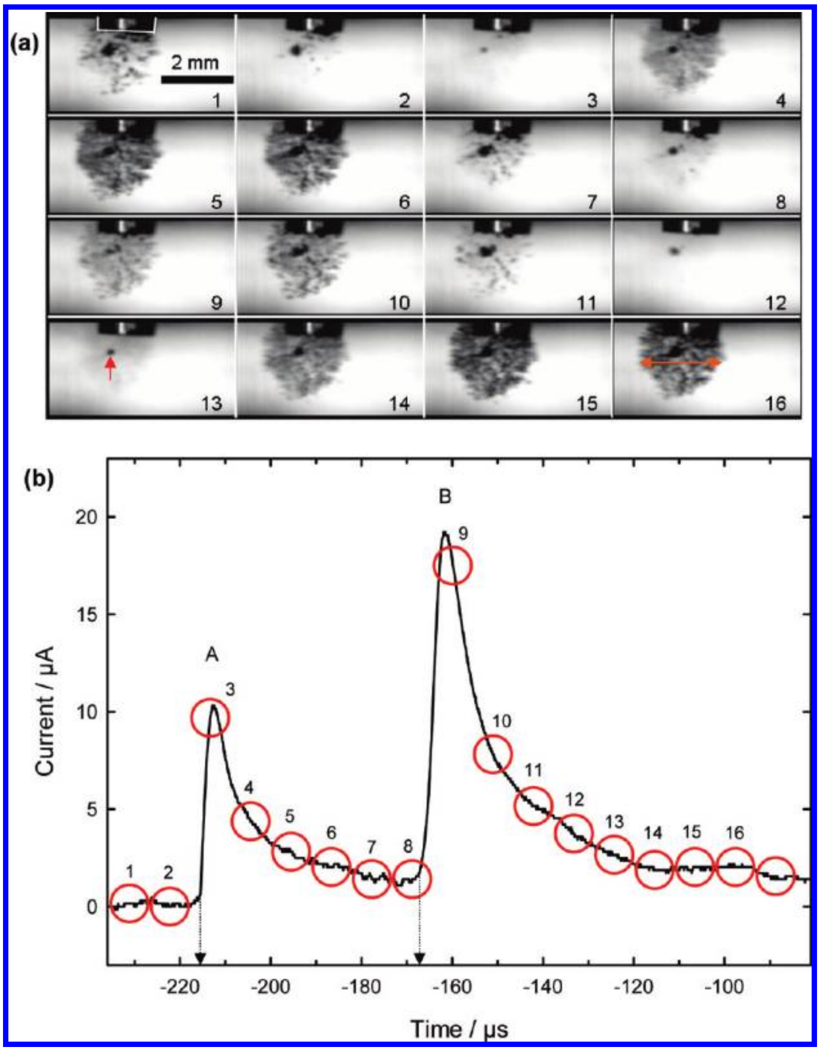

Figure 4. (a) High-speed video images and erosion events. Images recorded at 112,500 frames s^{-1} with a shutter speed of 1/112,500 s. (b) Plot showing two consecutive surface erosion/corrosion events (A and B) recorded on a 250 μm diameter aluminum electrode. The numbered circles represent the duration and position of the high-speed video images in (a) in relation to the current time transients shown in (b). The electrode was positioned centrally 80 mm from the base of the reactor which contained 1 dm^3 of 0.1 mol dm^{-3} Na_2SO_4 and held at 0 V vs a stainless steel counter/reference electrode. The reactor was driven at 22.81 kHz with a drive voltage amplitude of 150 V zero-to-peak (~250 kPa zero-to-peak amplitude). The arrows in frames 13 and 16 are to assist discussion in the text.

was found to be relatively low, in agreement with past studies.[34,39] However, even under these conditions the image-intensified camera is able to detect regions of luminescence (see Figure 2a for a single frame). However, it is also useful to 'stack and average' several frames recorded (normally at a rate of ~10 per second) consecutively to improve the signal-to-noise ratio and effectively increase the sensitivity of the technique by extending the exposure of the camera system. The effect of this software approach can be seen in Figure 2b. Note that Figure 2a shows an original image, whereas Figure 2b is the result of stacking and averaging 93 other images recorded at the same time, leading to a considerably clearer image. Nevertheless the position of the banding remains the same. These areas of high light emission were found to be ~35−40 mm apart and spaced regularly through the cell volume. As the frequency increased (Figure 2c−k), the boundary conditions are, for the most part, unchanged,[39] and so the top of the liquid column is always free of luminescence. Note that in Figure 2b there is little luminescence from the walls (denoted by the dotted lines), strong luminescence from the base of the cell where the light source is (blue arrow), and none from the top of the liquid (white arrow), where the pressure-release boundary conditions require that the acoustic pressure be zero at all times.[39] If this were a purely one-dimensional variation, then the distance from this pressure node to the first pressure antinode beneath the liquid surface would correspond to a quarter of an acoustic wavelength, allowing the effective sound speed in the cell to be estimated, and from this the void fraction of bubbles present (spatially averaged over the volume of the cell, assuming Wood's equation is valid[39,44]). However, this is not possible here from these images, as the mode shape is three-dimensional. Calculation of such mode shapes is not difficult for simple boundary conditions, but here the required *a priori* knowledge of the sound speed is not known.[39,41] However, with accurately modeled boundary conditions, the mode shape can be modeled and the sound speed inferred through comparison with measurement.[39] While the luminescence images are of use, they do not fully characterize the system in terms of yield or cavitational activity. A hydrophone (with an active cylindrical element of 6 mm × 6 mm) was scanned through the cell over a range of 100 mm along the vertical central axis of the cell and extending 25 mm from the center. This enables a pressure 'slice' to be recorded through the cell. Note at 92 kHz the band separation is the order of 7 ± 1 mm which is close to the size of the active element in the hydrophone (note the actual size of the hydrophone is included in each frame of Figure 2). Hence, spatial averaging

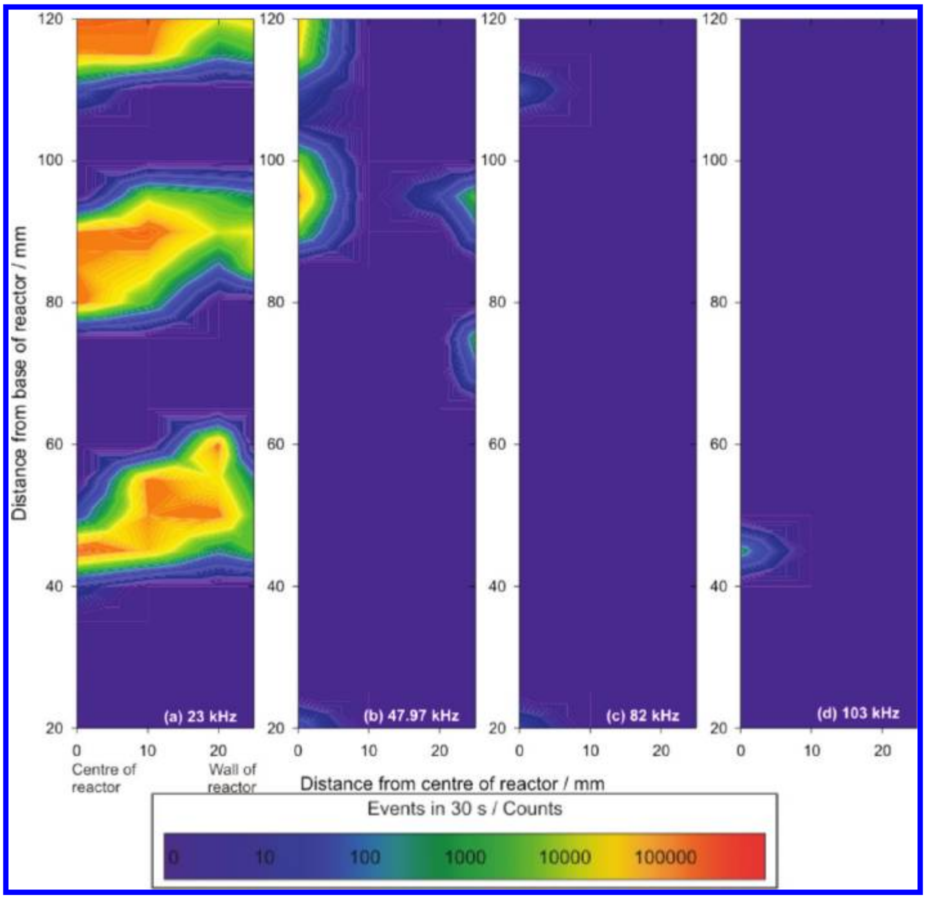

Figure 5. Contour plots of the surface erosion/corrosion event scans in the cylindrical reactor at 23, 47.97, 82, and 103 kHz in plots (a), (b), (c), and (d) respectively. All scans were conducted with a 250 μm Al electrode held at open circuit potential vs a stainless steel counter/reference electrode and the events collected using a multichannel analyzer with counting threshold set to 2.44 μA. Reactor contained 1 dm^3 of 0.1 mol dm^{-3} Na_2SO_4 and driven at 150 V (zero-to-peak amplitude, giving frequency-dependent pressure maps as shown in Figure 3).

will be significant under these conditions, and the peak pressure amplitudes will be underestimated. Figure 3 shows the results at four example frequencies, three of which (23, 47.97, and 82 kHz) exhibited strong luminescence, and one which did not (40 kHz). This enables a clear link between luminescent character and pressure amplitudes to be drawn. If the pressure amplitude is sufficiently high, inertial cavitation can be created (note this is in agreement with the theory derived by Holland and Apfel[13]). However, if the pressure amplitude is lower than this critical value (dependent on the solution, bubble population, and frequency), luminescent activity is not observed (as at 40 kHz, see Figure 3b). In the cases where luminescence and high pressure amplitudes are detected, Figure 3a for example, a set of horizontal bands centered on the axis of the cell are seen. In these regions the pressure amplitude is in excess of the inertial threshold (here estimated to be of the order of 110 kPa) with spatial peak pressure zero-to-peak amplitudes of ~250 kPa. Here, multibubble sonoluminescence (MBSL) is expected. This is in agreement with the results shown in Figure 2b where clear banding can be observed with a similar spacing to that predicted by the pressure map shown in Figure 3a (here a separation of 37 ± 4 mm was observed). Considering the higher frequencies, pressure banding can be observed; however, it is less distinct compared to that seen in Figure 3a. Clearly, the measurement of sufficient pressure amplitudes (in excess of the inertial limit) appears to indicate where one would expect to see luminescence (and hence cavitation activity). Figure 3e shows an MBSL image for this cylindrical reactor and the corresponding pressure map (both half slices) at 92 kHz acoustic excitation. Regions of high luminescence coincide with high acoustic pressure amplitude detected by the hydrophone as expected. The frequency response of activity is therefore a combination of the frequency response of the source and the vessel, and the way these two together provide a baseline for the inhomogeneities and local amplitudes of the pressure in the liquid (where, for example, the direct field from the horn decays in a predictable manner[31] but excites modes within the vessel[34,39]). This baseline field is in turn modified by (and modifies) the bubble population, including its distribution and cavitational activity.[1,39] It is desirable to map their distribution, if one is to compare like-with-like when the results at different frequencies are compared. When such measurements are undertaken, as in the current study, they prove to be invaluable in explaining the actual sources of frequency dependence observed. Nevertheless, there are limitations to both the pressure and luminescence measurement strategies. For example, luminescence requires black-out conditions and expensive image-intensified cameras, while hydrophones, (owing to their finite size, bandwidth, and uncalibrated phase response) have a limited range of frequencies over which they can operate without significant spatial averaging or other errors being observed. Therefore, as an alternative approach, we have used an electrochemical erosion/corrosion approach to this problem. In this case we employed an aluminum electrode held in a passive state. Under these conditions erosion/corrosion effects associated with cavitation phenomena can be detected. This approach has some advantages. For example it employs relatively small electrodes (electrode support ~1.5 mm in diameter, while the active area is 4.9 × 10^{-4} cm^2) and produces no signal in the absence of a suitable erosive mechanism (e.g., an inertial cavitation event).[31−33,43] In order to show how this

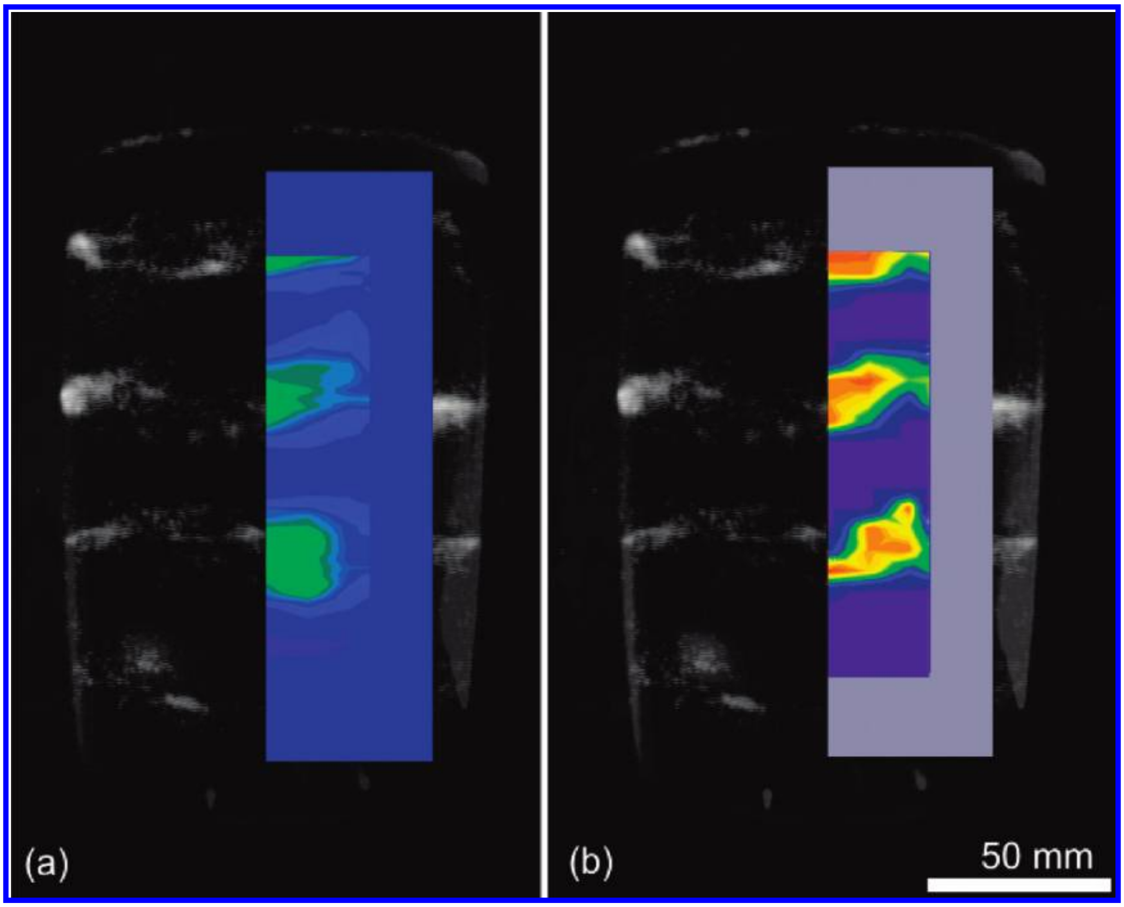

Figure 6. Composite image of the cylindrical reactor showing the intensified MBSL light emission images when driven at 23 kHz (images a and b, black and white portions) with the corresponding acoustic pressure contour map (image a, color portion) and logarithmic surface event contour map (image b, color portion) to show the correlation between the measurements.

device operates in this cell, a set of high-speed images were simultaneously recorded with erosion/corrosion transients recorded by an electrode (here an aluminum disk 250 μm in diameter). Figure 4a shows a set of frames recorded of the electrode (highlighted by a white surround in frame 1) within the cell (Note: this is the ~1.5 mm diameter body of the electrode, the electrode itself being a 250 μm diameter aluminum disk sealed within this body). The images show the growth and collapse of a cluster[45−47] of cavitation bubbles around the electrode. Interestingly, this cluster of events appears to center around one slightly larger 'resident' bubble (highlighted by a red arrow in frame 13). The cluster grows and collapses with a period corresponding to 5 ± 1 frame. This corresponds to 44.4 ± 8.9 μs. This is close, within experimental error, to the period of the sound field employed (22.81 kHz) which is 43.8 μs. The cluster appears to consist of a multitude of small bubbles emanating from the central event. At its maximum the cluster extends to a diameter of 2.3 mm (as shown by the arrow; see frame 16). The electrode can detect the effects of this cluster of events as erosion of the surface (and the corresponding electrochemical event associated with the corrosion of the damaged interface). Note the erosion of the surface of the electrode is detected as an anodic current time transient. This is detected as the surface repassivates (an oxide layer is reformed in this case) under electrochemical control. Further details describing this method can be found elsewhere.[31−33,42,43] In the time period shown in Figure 4, two erosion/corrosion events were recorded 48 ± 3 μs apart (see Figure 4b). Interestingly, erosion is associated with the apparent disappearance of the cluster because the erosion/corrosion event is detected when the cluster bubbles collapse to a size too small to image.[24,25] This occurs in frames 2/3 and 7/8 (note the dynamics of these collapses are rapid in comparison to the shutter speed and frame rate employed; hence, we are only able to associate the erosion with cluster collapse and not give an exact timing from the imaging data alone). Finally, erosion was not detected by the electrode for the cluster collapse observed in frames 12/13. This observation implies that under these conditions an erosive event may not always be detected as either the magnitude of the effect varies (indeed the size of the events change with time—see Figure 4) or the location of the cluster center varies with time with respect to the electrode center. However, the erosion detection is clearly linked with bubble action close to the aluminum electrode as expected. This electrochemical approach can hence be employed to map regions of erosion (for example this will be important if this mechanism is desired for surface cleaning).

Figure 5 shows mapping of erosion/corrosion events within the cylindrical reactor. Here the electrode was positioned in the rZ plane (corresponding to the vertical (Z) and horizontal (r) motion from the center of the cell). In each position erosion/corrosion events were recorded for a period of 30 s. The data gathered in this manner were used to create the contour maps shown in Figure 5. Plots a−d of Figure 5 show the data obtained at 23, 47.97, 82, and 103 kHz respectively. These frequencies where chosen to match regions of high MBSL luminescence (see Figure 2) and high acoustic pressure amplitude (see Figure 3). Interestingly, at 23 kHz (Figure 5a) a distinct band structure can be seen in the erosion/corrosion data. However, at higher frequencies (e.g., 47.97, 82, and 103 kHz), although some

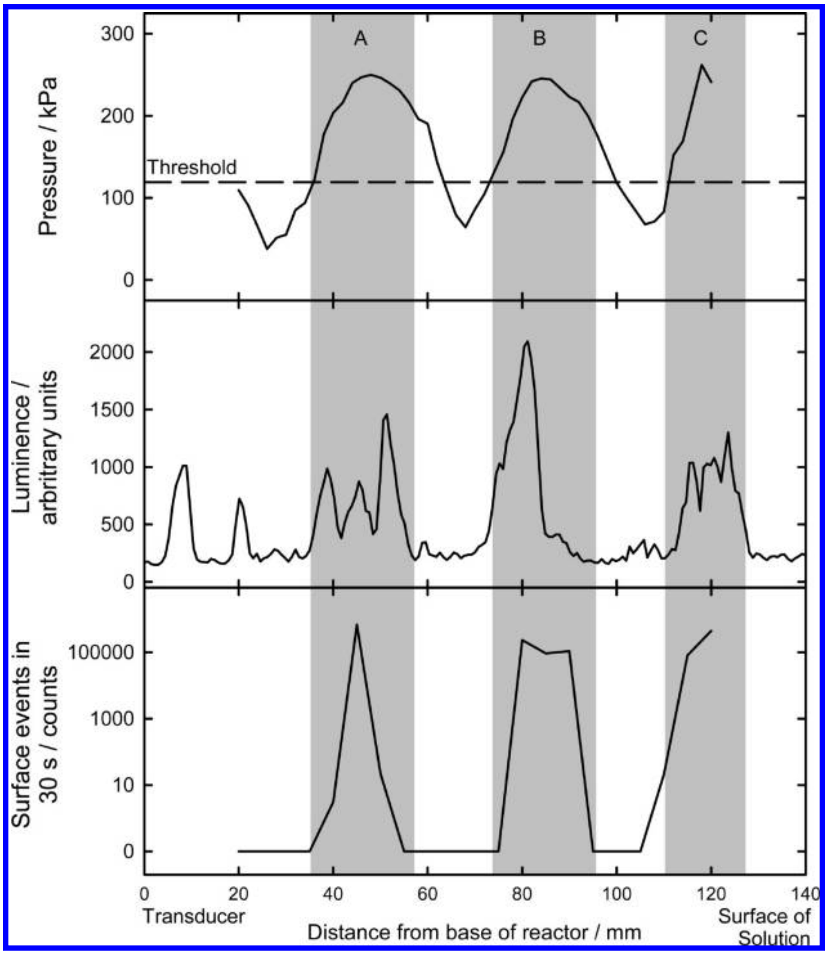

Figure 7. Plot comparing the central pressure scan and luminance trace from reactor 4 driven at 23 kHz as a function of distance with three bands of increased activity identified (a, b, and c). Pressure trace consisting of a 50-point scan with a resolution of 2 mm. Luminance trace calculated from low-light image using Matlab. Surface scan consisting of 20 points, with 5 mm resolution, conducted with a 250 μm Al electrode 0 V vs a stainless steel counter/reference electrode. Events collected using a multichannel analyzer with counting threshold set to 2.44 μA. For all measurements the reactor contained 1 dm^3 of 0.1 mol dm^{-3} Na_2SO_4 driven at 150 V (zero-to-peak amplitude).

erosion signal is apparent, a distinct band structure was not observed. This presumably relates to the dynamics of the cavitation events produced. It also coincides with an observation by ear that audible noise is most dramatic at 23 kHz, indicating strong subharmonic emission and presumably inertial event generation (see Figure 4 for cluster events).

Figure 6 shows how MBSL light emission, acoustic pressure amplitude, and erosion/corrosion data correlate at 23 kHz. Clearly a strong correlation exists under these conditions. However, this is not the case at higher frequencies where the erosion/corrosion data fail to pick up strong band structure. Note, this is not a limitation with the electrochemical technique but an indication of a change in the nature of the cavitation field. Clearly, at lower frequencies strong erosive mechanisms are generated under the conditions employed while at higher acoustic frequencies (for example 82 kHz) although strong light emission is observed (correlating to significant acoustic pressure amplitudes), erosive mechanisms are less common. Figure 4 has shown that the time-resolved erosion/corrosion of the surface is linked to the dynamics of cluster collapse. In turn this is known to be dependent on the cluster itself.[46,47] While at ~23 kHz it appears that these cluster events are generated within the cylindrical cell, at higher frequencies the lack of consistent erosion/corrosion events indicate that these clusters may be harder to maintain and generate. This poses some interesting questions. For example the type of cavitation that exists within sonochemical cells has received attention.[38,48,49] These studies suggest that the acoustic emission and the sonochemical properties of a particular cell are associated with transient (inertial) and stable (noninertial) cavitation. The results reported here suggest that, at the lower frequency range studied (e.g., ~23 kHz), clusters of events are present. However, at the high frequency range studied, the absence of persistent erosion/corrosion events suggests that cluster collapses are less prevalent around the electrode. Clearly an interesting aside from these observations relates to the effect of cluster events on luminescence, acoustic emission, and sonochemistry. This is beyond of the scope of the current paper and will be dealt with elsewhere.

Finally Figure 7 shows a direct quantitative comparison of the measurements made at 23 kHz, produced by scanning along the axis of the cylindrical cell. In Figure 7, regions A, B, and C indicate locations in the liquid along the cylinder axis where significant luminescence, surface erosion/corrosion, and acoustic pressure amplitude were observed. Included in the upper panel of the figure is an estimation (made using the method described elsewhere[33]) of the acoustic pressure threshold that would generate inertial cavitation were the appropriate size of seed cavitation nucleus be present. While effects linked to inertial cavitation are only observed when the pressure exceeds the inertial limit, they are not always observed in these regions. This further illustrates a significant point. In order for cavitation effects to be observed, all the relevant conditions must be satisfied. This is predominantly related to the inertial limit (which in turn reflects the solution parameters) but is also linked to the presence of suitable bubble nuclei within the system. Hence, even though the allowable bubble nucleus size range for incepting inertial cavitation at these low kHz frequencies is much broader than that required for higher frequencies, the presence of a suitable population of nuclei cannot be guaranteed. Inclusion of this factor, and others such as bubble−bubble interactions and the role of cluster collapses in influencing the particular parameter being measured (see Figure 4), place limitations on our current abilities to predict the occurrence and extent of inertial cavitation and the range of effects it can generate.

Conclusions

A study using a variety of sensing techniques of a cylindrical cell has been presented. Characterization of the sound field through both luminescent and acoustic measurements suggests a strong, but frequency-dependent system. These results not only confirm previous reports on similar cylindrical (glass-jacketed) cells[39,50] but also extend our knowledge to an assessment of time-resolved erosion/corrosion within this sound field. The erosion/corrosion mapping has shown that the sound field also dominated the erosion/corrosion patterns within this environment at 23 kHz. In addition, cluster collapse close to the electrode surface was observed and correlated to the erosion/corrosion events detected. The correlation between pressure mapping, luminescence, and erosion is less distinct as the frequency of the sound field is raised to high-order modes. This indicates that less erosion, which in turn was shown to be related to cluster collapse, is generated in the higher-order modes.

Acknowledgment. We thank Mark Hodnett and Bajram Zeqiri for useful discussion and NPL for partial funding of C.J.B.V. and the EPSRC (EP/D05849X/1) for funding for the high-speed camera.

References and Notes

(1) Leighton, T. G. *The Acoustic Bubble*; Academic Press: London, 1994.

(2) Hoffmann, M. R.; Hua, I.; Hoechemer, R. *Ultrason. Sonochem.* **1996**, *3*, s163.

(3) Leighton, T. G. *Prog. Biophys. Mol. Biol.* **2007**, *93*, 3.

(4) Lea, S. C.; Price, G. J.; Walmsley, A. D. *Ultrason. Sonochem.* **2005**, *12*, 233.

(5) O'Leary, R.; Sved, A. M.; Davies, E. H.; Leighton, T. G.; Wilson, M.; Kieser, J. B. *J. Clin. Periodontol.* **1997**, *24*, 432.

(6) Leighton, T. G.; Cleveland, R. O. *J. Eng. Med.* **2010**, *224* (2), 317.

(7) Leighton, T. G.; Birkin, P. R.; Hodnett, M.; Zeqiri, B.; power, J. F.; Price, G. J.; Mason, T.; Plattes, M.; Dezhkunov, N.; Coleman, A. Cavitation of measurements of reference acoustic cavitation (COMORAC): An experimental feasibility trial. In *Bubble and Particle Dynamics in Acoustic Fields: Modern Trends and Applications*; Doinikov, A. A., Ed.; Research Signpost: Kerala, India, 2005; p 37.

(8) Leighton, T. G. *The Acoustic Bubble*; Academic Press: London, 1994; Section 4.3.1.

(9) Apfel, R. E. Some new results on cavitation threshold prediction and bubble dynamics. In *Cavitation and Inhomogeneities in Underwater Acoustics*; Lauterborn, W., Ed.; Springer: New York, 1980.

(10) Apfel, R. E. In *Methods in Experimental Physics*; Edmonds, P. D., Ed.; Academic Press: New York, 1981; Vol. 19.

(11) Apfel, R. E.; Holland, C. K. *Ultrasound Med. Biol.* **1991**, *17*, 179.

(12) Apfel, R. E.; Holland, C. K. *Ultrasound Med. Biol.* **1991**, *17*, 179.

(13) Holland, C. K.; Apfel, R. E. *IEEE Trans. Ultrason. Ferroelectr. Freq. Control* **1989**, *36*, 204.

(14) Didenko, Y. T.; Suslick, K. S. *Nature* **2002**, *418*, 394.

(15) Eddingsaas, N. C.; Suslick, K. S. *J. Am. Chem. Soc.* **2007**, *129*, 3838.

(16) Flint, E. B.; Suslick, K. S. *Science* **1991**, *253*, 1397.

(17) Suslick, K. S. *Science* **1990**, *247*, 1439.

(18) Suslick, K. S.; Doktycz, S. J.; Flint, E. B. *Ultrasonics* **1990**, *28*, 280.

(19) Suslick, K. S.; Hammerton, D. A.; Cline, R. E. *J. Am. Chem. Soc.* **1986**, *108*, 5641.

(20) Šponer, J. *Stud. Biophys.* **1990**, *137*, 91.

(21) Šponer, J. *Ultrasonics* **1991**, *29*, 376.

(22) Šponer, J.; Davadorzh, C.; Mornstein, V. *Stud. Biophys.* **1990**, *137*, 81.

(23) Leighton, T. G. *Ultrason. Sonochem.* **1995**, *2*, S123.

(24) Leighton, T. G. *Ultrasonics* **1989**, *27*, 50.

(25) Leighton, T. G.; Walton, A. J.; Field, J. E. *Ultrasonics* **1989**, *27*, 370.

(26) Yasui, K.; Iida, Y.; Tuziuti, T.; Kozuka, T.; Towata, A. *Phys. Rev. E* **2008**, *77*.

(27) Leighton, T. G.; Cox, B. T.; Phelps, A. D. *J. Acoust. Soc. Am.* **2000**, *107*, 130.

(28) Leighton, T. G.; Ho, W. L.; Flaxman, R. *Ultrasonics* **1997**, *35*, 399.

(29) Leighton, T. G.; Pickworth, M. J. W.; Walton, A. J.; Dendy, P. P. *Phys. Med. Biol.* **1988**, *33*, 1239.

(30) Leighton, T. G.; White, P. R.; Morfey, C. L.; Clarke, J. W. L.; Heald, G. J.; Dumbrell, H. A.; Holland, K. R. *J. Acoust. Soc. Am.* **2002**, *112*, 1366.

(31) Birkin, P. R.; Offin, D. G.; Joseph, P. F.; Leighton, T. G. *J. Phys. Chem. B* **2005**, *109*, 16997.

(32) Birkin, P. R.; Offin, D. G.; Leighton, T. G. *Electrochem. Commun.* **2004**, *6*, 1174.

(33) Birkin, P. R.; Offin, D. G.; Leighton, T. G. *Phys. Chem. Chem. Phys.* **2005**, *7*, 530.

(34) Birkin, P. R.; Power, J. F.; Vinçotte, A. M. L.; Leighton, T. G. *Phys. Chem. Chem. Phys.* **2003**, *5*, 4170.

(35) Fang, X.; Mark, G.; von Sonntag, C. *Ultrasonic Sonochemistry* **1996**, *3*, 57.

(36) Mark, G.; Tauber, A.; R.; Laupert; Schuchmann, H. P.; Schulz, D.; Mues, A.; von Sonntag, C. *Ultrason. Sonochem.* **1998**, *5*, 41.

(37) von Sonntag, C.; Mark, G.; Tauber, A.; Schuchmann, H.-P. *Advances in Sonochemistry*; JAI Press; Greenwich, CT, 1999; Vol. 5; pp 109.

(38) Ashokkumar, M.; Hodnett, M.; Zeqiri, B.; Grieser, F.; Price, G. J. *J. Am. Chem. Soc.* **2007**, *129*, 2250.

(39) Birkin, P. R.; Leighton, T. G.; Power, J. F.; Simpson, M. D.; Vinçotte, A. M. L.; Joseph, P. F. *J. Phys. Chem. A* **2003**, *107*, 306.

(40) Baik, K.; Jiang, J.; Leighton, T. G. *J. Acoust. Soc. Am.* **2010**. Under review.

(41) Fox, F. E.; Curley, S. R.; Larson, G. S. *J. Acoust. Soc. Am.* **1955**, *27*, 537.

(42) Birkin, P. R.; O'Connor, R.; Rapple, C.; Silva-Martinez, S. *J. Chem. Soc., Faraday Trans.* **1998**, *94*, 3365.

(43) Birkin, P. R.; Offin, D. G.; Leighton, T. G. *Wear* **2005**, *258*, 623.

(44) Leighton, T. G. G.; Robb., B. N. *J. Acoust. Soc. Am.* **2008**, *124*, EL313.

(45) Vyas, B.; Preece, C. M. *J. Appl. Phys.* **1976**, *47*, 5133.

(46) Hansson, I.; Kedrinskii, V.; Morch, K. A. *J. Phys. D: Appl. Phys.* **1982**, *15*, 1725.

(47) Hansson, I.; Morch, K. A. *J. Appl. Phys.* **1980**, *51*, 4651.

(48) Price, G. J.; Ashokkumar, M.; Hodnett, M.; Zequiri, B.; Grieser, F. *J. Phys. Chem. B* **2005**, *109*, 17799.

(49) Ashokkumar, M.; Lee, J.; Iida, Y.; Yasui, K.; Kozuka, T.; Tuziuti, T.; Towata, A. *Phys. Chem. Chem. Phys.* **2009**, *11*, 10118.

(50) Birkin, P. R.; Power, J. F.; Abdelsalam, M. E.; Leighton, T. G. *Ultrason. Sonochem.* **2003**, *10*, 203.

JP1027977